Influence of impulse characteristics on realizing high-energy orbits in hybrid energy harvester

Jerzy MARGIELEWICZ, Damian GĄSKA
Silesian University of Technology, Faculty of Transport and Aviation Engineering, Krasińskiego 8, Katowice 40-019, Poland
Grzegorz LITAK, Piotr WOLSZCZAK
Lublin University of Technology, Faculty of Mechanical Engineering, Nadbystrzycka 36, Lublin 20-618, Poland
Daniil YURCHENKO
Institute of Sound and Vibration Research, University of Southampton, Southampton, SO17 1BJ, UK

Abstract: Energy harvesters based on non-linear systems are promising devices for extracting energy from mechanical vibrations. This paper presents a new design of energy harvester consisting of two coupled nonlinear systems; the Duffing oscillator and a system with quasizero stiffness. A numerical analysis of the dynamics of the harvester is carried out, presenting coexisting solutions and their energy efficiencies in both chaotic and periodic motion zones. The root mean squared (RMS) voltage results depend on the dimensionless excitation frequency, where high-energy orbits are coexisting with low-energy orbits. Therefore, the second part of the paper focuses on various strategies for jumps between the orbits using impulses. Different impulse characteristics and their sequences for periodic and chaotic zones are analyzed. Therefore, a detailed analysis is presented for many strategies using an impulse excitation diagram (IED) as a numerical tool for accurately estimating the amplitude of the impulse, its duration, and the moment of initiation. The probability of achieving a given solution is also determined. The simulation results show that achieving the most effective orbit with a single impulse, as well as several impulses, requires similar energy. However, the advantage of the step-by-step method is the lower energy required to initiate a single impulse which enables the use of a smaller regulator. This work can be a valuable tool for designing various systems and strategies for changing the orbit of a solution.

Keywords: multiple solutions, energy efficiency, orbit jump, high-energy orbit, nonlinear dynamics, energy harvesting.

Highlights

Hybrid energy harvester with quasizero system is designed.
Different strategies for orbit jump using impulses are proposed and summarized.
A step-by-step method of correcting solutions is proposed.
Coexistence of chaotic and periodic solutions are checked.
Various parameters of quasizero system were analyzed.

1. Introduction

Scientific research related to energy harvesting has been developing since the beginning of the 21st century. Initially, energy harvesters were simple devices designed to recover energy lost through mechanical vibrations, temperature changes, airflow, etc. [1,2]. However, until 2009, they were designed and tested as linear systems where the effective range of energy recovery was limited to the resonance frequencies of the vibration source. More than ten years ago researchers [3–5] proposed the introduction of non-linearity into energy harvesters, leading to them being characterized by a wider frequency range, allowing for effective energy recovery. Consequently, researcher interests have followed this direction and non-linearities are now obtained primarily using magnets [6–8], elastic and dissipative elements [9–11], special construction of cantilever beams [12,13], etc. In most cases, such systems are based on a cantilever beam with an attached piezoelectric, allowing the mechanical energy of beam vibrations to be converted into electricity [14,15]. Energy harvesters usually handle small devices and the value of the recovered

energy; however, they should be capable of powering sensors, simple measurement systems, and transmitting information [16–19]. Such solutions are applicable wherever access to electricity is difficult or expensive. Battery power is not preferred due to the need to replace them.

The most important element of energy harvesting devices is obtaining design solutions that maximize energy efficiency. The main challenge of this is the implementation of high-energy orbits [20,21]. For nonlinear multi-stable systems many solutions occur for the same excitation conditions, especially for low-frequency, high-level excitations. Unfortunately, for zero initial conditions, these systems often deal with vibrations in the range of low-energy orbits, leading to a reduction in the energy that can be harvested [22]. If the initial conditions could be controlled (steered) using mechanical or electrical methods to obtain high-energy orbits regardless of the excitation conditions, then a high energy efficiency of the designed energy harvester would be achieved [7,23,24]. However, regardless of the method, a system that allows jumps between orbits also needs energy, but the key question is how much energy would be required [25,26]. If the harvested energy is lower than the energy required to change the orbit, the system will not fulfill its task. Therefore, it is necessary to accurately estimate the amount of required energy and design an appropriate energy harvester.

Based on scientific research, there are currently two main methods of changing the orbit. These are either electrical or mechanical methods consisting of 'kicking' the system via an external force. One of the methods was presented by Sebald et al. He proposed a technique called fast burst perturbation [27] which consists of a fast voltage burst applied to the piezoelectric element. Wang presents the load perturbation method [28] based on electrical load effects, which enabled a several-fold increase in energy harvesting efficiency. A voltage impulse perturbation approach [29] based on negative resistance was presented by Lan et al. Similar studies and examples of this method are also presented in other works [28,30]. Mechanical methods, however, are based on an external mechanical input. Zhou et al. presented an impact-induced method [31] for nonlinear energy harvesters. The possibilities of using buckling level modification are explored within bistable energy harvesters [23,32]. Yan et al. show a low-cost orbit jump method via energy-efficient transient stiffness modulation [26].

Regarding the discussed research results, methods of changing the solution orbit, and development of high-energy orbits within nonlinear energy harvesters, it can be concluded that they improve energy efficiency, but are often limited to one design. Therefore, the work in this paper has been divided into two main parts. First, in chapters 2 and 3, a new example of energy harvester is presented. The design is based on the Duffing oscillator and the quasizero energy harvester (QZEH). Secondly, presented in sections 3.1 to 3.5, further research is carried out with a numerical analysis for the possibility of changing the solution orbit by presenting several strategies for using impulses. For this, a new tool called Impulse Excitation Diagram (IED) is proposed. The impulse strategies and IEDs proposed are universal tools that enable the optimization of the duration, initiation point, and amplitude of the impulse for higher energy orbit jumps, using electrical and mechanical methods.

2. Mathematical model formulation

The tested energy harvesting structure consists of two coupled nonlinear systems: the Duffing oscillator, and the system with quasizero stiffness, which is similar to the quasizero energy harvester QZEH [24,33]. In the numerical experiments, it was assumed that

the analyzed system is influenced by the external harmonic excitation, $y_0 = Asin(\omega_W t)$, coming from the vibrating device, *V*, where the energy harvesting system is attached using the *VI* screws, shown in Fig. 1. The system with quasizero stiffness consists of the spring and damping elements, c_{K1}, c_{K2}, c_G, b_G, and inertial element, m_2, which is connected to the Duffing oscillator, *III,* via a flexible beam, *I*. In the interests of clarity, the quasizero stiffness model is simplified in Figure 1a. It is mapped by the equivalent nonlinear elastic element, c_Z, and dissipative b_Z, while its detailed structure is presented in Figure 1b. Piezoelectric transducers, *II*, which transform mechanical energy into electricity, are glued onto the flat surfaces of the flexible beam, *I*, which is attached to the Duffing oscillator via the *IV* screw. Due to the deformation of the cantilever beam, a voltage is induced on the piezoelectric electrodes.

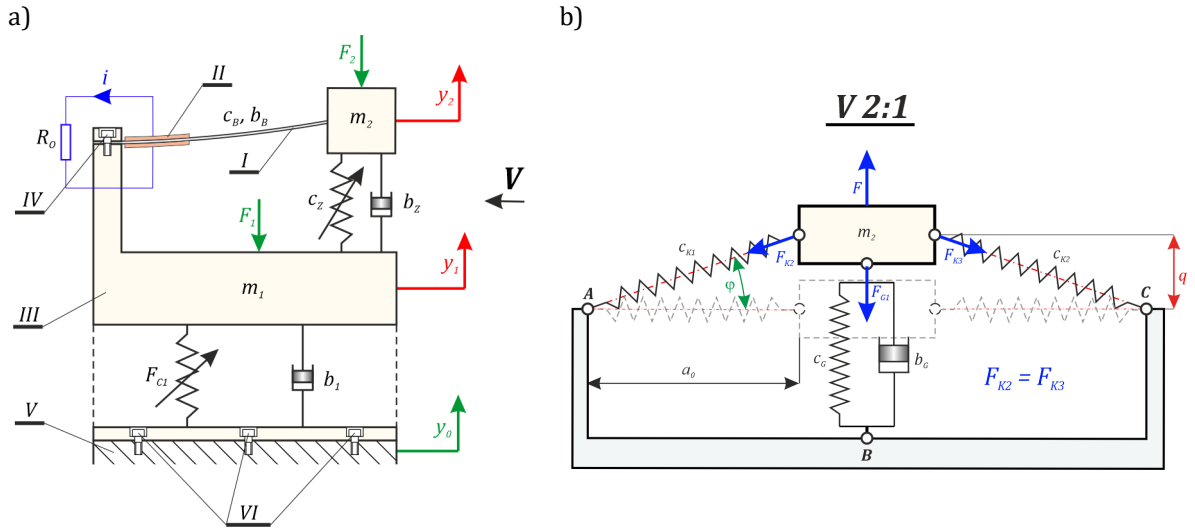

Fig. 1. Tested system: a) schematic diagram of a hybrid energy harvester consisting of a duffing oscillator and quasizero energy harvester (QZEH), b) quasizero stiffness system – this is a side view of upper part of Fig1a. *I* – flexible beam, *II* – piezoelectric transducer, *III* – duffing oscillator, *IV, VI* – screws, *V* – vibrating device.

During the numerical experiments, a symmetrical structure of connections of quasizero system elastic elements was assumed, attached at points A, B and C to the Duffing *III* type oscillator, shown in Fig.1b. From a mathematical aspect, the energy dissipating elements b_B and b_G form parallel connections. Therefore, a simplification was made consisting of the introduction of equivalent dissipation elements: $b_Z = b_B + b_G$. A similar situation occurs for elastic elements modeling the stiffness of flexible beams c_B, and the main spring, c_G. Here, the elastic elements of the energy harvesting system are mapped via linear mechanical characteristics.

The external dynamic loads, F_1 and F_2, which affect the inertia elements of the hybrid energy harvesting system, reflect the impulse excitation for high-energy orbit jump. The characteristics of the impulse interactions were described using half of the sinusoidal function. Therefore, numerical experiments will be carried out, aiming to directly affect the response of the tested energy harvesting system.

2.1. Identification of the mechanical characteristics of the QZEH system

The potential barrier to systems with quasizero stiffness is defined by the main spring, c_G, and the compensation springs, c_{K1} and c_{K2}, which are related to the inertia elements, m_2. In equilibrium, the axes of the compensation springs are orientated parallel to the

straight line defined by points *A* and *C,* shown in Fig. 1b. The equivalent dissipation element, b_Z, present in the energy harvesting system, models the energy losses related to the deformation of the flexible beam, *I*, and accounts for the resistances in the articulated joints of the compensation springs. Based on the adopted schematic diagram in Fig. 1b, the cause-and-effect relations between the displacement of the inertial element, *q*, and the external load, *F*, were derived. When deriving the static characteristics of the system with quasizero stiffness, the influence of inertia and dissipation forces is neglected. The external load, *F*, acting on the inertial element, is balanced by the forces induced in the main spring, c_G, and compensation springs whose stiffness coefficients are represented by the formula $c_K = c_{K1} + c_{K2}$:

$$F(q) = F_{G1} + 2F_{K2}sin\varphi = c_G q + 2(F_{20} + c_K \Delta L)\frac{q}{\sqrt{a_0^2 + q^2}}, \quad a_0 > 0. \tag{1}$$

In equation (1), F_{20} represents the preload of the compensation springs. Appropriate analytical relationships were derived with respect to the reference system, which begins at point A in Fig. 1b. The quasizero stiffness system is characterized by a symmetrical configuration, therefore it is sufficient to know the relationship that defines the change in the length of one compensating element:

$$\Delta L = \sqrt{a_0^2 + q^2} - \sqrt{a_0^2}. \tag{2}$$

Substituting equation (2) into (1) leads to the equation defining the static characteristics of a system with quasizero stiffness:

$$F(q) = c_G q + 2\left(F_{20} + c_K\left(\sqrt{a_0^2 + q^2} - \sqrt{a_0^2}\right)\right)\frac{q}{\sqrt{a_0^2 + q^2}}. \tag{3}$$

The proper functioning of the system, and ensuring a flat energy potential well, depends on the appropriate selection of the initial stress of the compensation springs, F_{20}. To identify this, equation (3) was differentiated with respect to the generalized coordinate:

$$c(q) = \frac{\partial F(q)}{\partial q} = c_G + \frac{2c_K q^2}{a_0^2 + q^2} - \frac{2q^2\left(F_{20} + c_K\left(\sqrt{a_0^2 + q^2} - \sqrt{a_0^2}\right)\right)}{\left(\sqrt{a_0^2 + q^2}\right)^3} + \frac{2\left(F_{20} + c_k\left(\sqrt{a_0^2 + q^2} - \sqrt{a_0^2}\right)\right)}{\sqrt{a_0^2 + q^2}}. \tag{4}$$

Assuming a zero, or a close to zero stiffness of the quasizero stiffness system, equation (4) equates to zero, $c(q = 0) = \frac{\partial F}{\partial q} = 0$ and has zero displacement of the inertial element, $q = 0$. After considering the above assumptions, the tension of the compensation springs takes the following form:

$$F_{20} = -\frac{c_G\sqrt{a_0^2}}{2}. \tag{5}$$

The mechanical characteristic describing the relationship between the deflection q, and the external load, F, is given by the equation:

$$F(q) = \underbrace{(c_G + 2c_K)}_{c_Z}\left(1 - \frac{\sqrt{a_0^2}}{\sqrt{a_0^2 + q^2}}\right)q. \tag{6}$$

The relationship defining the potential barrier is obtained by integrating equation (6) with respect to the generalized coordinate, q:

$$V(q) = \int F(q)dq = \frac{c_Z}{2}\left(a_0 - \sqrt{a_0^2 + q^2}\right)^2. \tag{7}$$

Equation (7) shows that the characteristics of the potential barrier are influenced by two parameters: the equivalent stiffness, c_Z, and the geometric quantity, a_0. Based on these dependencies, graphs were drawn to illustrate the influence of the equivalent stiffness, c_Z, and the design parameter, a_0, on the potential barriers of the system with quasizero stiffness. The characteristics of the potential barrier were illustrated against the Duffing oscillator potential barriers (dashed lines), where the well depth was used as the control parameter. Γ represents the scaling parameter through which the depth of the potential barrier well was mapped – introduced in Eq. (8).

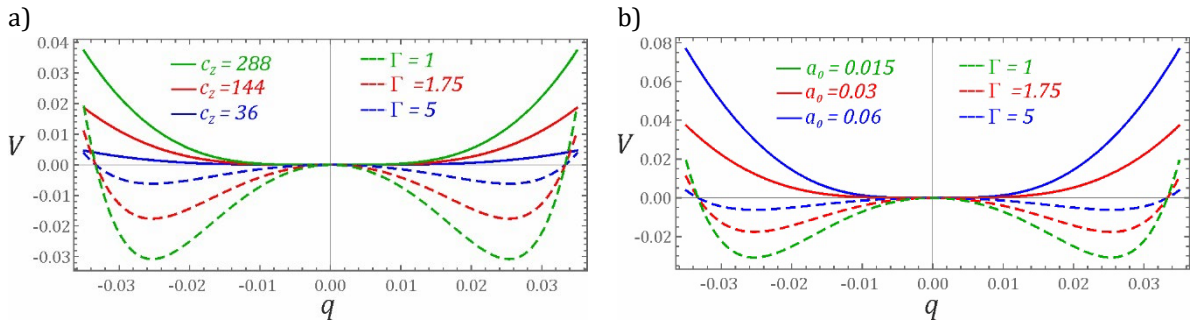

Fig. 2. The results of numerical calculations showing the influence of the parameters: a) equivalent stiffness c_Z, b) geometric quantity a_0. Γ represents the scaling parameter through which the depth of the potential barrier well was mapped.

The results presented in Fig. 2 show that the increase in the equivalent stiffness coefficient c_Z causes the limitation of the zone with a potential close to zero. However, the situation is the opposite regarding the parameter, a_0, where increasing its value causes a flattening of the potential well. The identified static characteristics are the basis for quantitative and qualitative computer simulations.

2.2. Dimensionless mathematical model of the energy harvesting system

The kinematic force acts via the parallel connection of the nonlinear elastic element, $F_{C1} = -c_1(y_1 - y_0) + c_2(y_1 - y_0)^5$, with the linear damper, b_1, on the inertia element of

the Duffing type oscillator, m_1. The differential equations of motion resulting from the formulated phenomenological model, shown in Fig. 1a, take the following form:

$$\begin{cases} m_1\dfrac{d^2y_1}{dt^2}+b_1\left(\dfrac{dy_1}{dt}-\dfrac{dy_0}{dt}\right)-b_Z\left(\dfrac{dy_2}{dt}-\dfrac{dy_1}{dt}\right)-c_{11}(y_1-y_0)+c_{12}(y_1-y_0)^5- \\ c_Z\left(1-\dfrac{\sqrt{a_0^2}}{\sqrt{a_0^2+(y_2-y_1)^2}}\right)(y_2-y_1)=F_1, \\ m_2\dfrac{d^2y_2}{dt^2}+b_Z\left(\dfrac{dy_2}{dt}-\dfrac{dy_1}{dt}\right)+c_Z\left(1-\dfrac{\sqrt{a_0^2}}{\sqrt{a_0^2+(y_2-y_1)^2}}\right)(y_2-y_1)+k_Pu=F_2, \\ C_P\dfrac{du}{dt}+\dfrac{1}{R_P}u-k_P\left(\dfrac{dy_2}{dt}-\dfrac{dy_1}{dt}\right)=0, \end{cases} \tag{8}$$

where:

$c_{11}=\frac{c_1}{\Gamma}, c_{11}=\frac{c_2}{\Gamma}$, and Γ represents the scaling parameter through which the depth of the potential barrier well was mapped.

After introducing new coordinates, $q_1=y_1-y_0,\ q_2=y_2-y_1$, and several transformations, the mathematical model of the hybrid energy harvesting system takes the following form:

$$\begin{cases} \ddot{x}_1+\delta_2\dot{x}_1-\delta_3\dot{x}_2-\gamma(x_1-\alpha x_1^5)-\dfrac{1}{\mu}\left(1-\dfrac{1}{\sqrt{1+{x_2}^2}}\right)x_2=\omega^2psin(\omega\tau)+p_1, \\ \ddot{x}_2+\delta_1\dot{x}_2+\left(1-\dfrac{1}{\sqrt{1+{x_2}^2}}\right)x_2+\vartheta u=\omega^2psin(\omega\tau)+p_2-\ddot{x}_1, \\ \dot{u}+\kappa u-\theta\dot{x}_2=0, \end{cases} \tag{9}$$

where:

$$\mu=\frac{m_1}{m_2},\quad \delta_1=\frac{b_Z}{\omega_0 m_2},\quad \delta_2=\frac{b_1}{\mu\omega_0 m_2},\quad \delta_2=\frac{b_Z}{\mu\omega_0 m_2},\quad \alpha=\frac{c_{12}a_0^4}{c_{11}},\quad \omega_0^2=\frac{c_Z}{m_2},$$
$$\eta=\frac{c_{11}}{c_Z}\quad \gamma=\frac{\eta}{\mu},\quad \omega=\frac{\omega_W}{\omega_0},\quad \tau=\omega_0 t,\quad p=\frac{A}{a_0},\quad p_1=\frac{F_1}{a_0c_Z\mu},\quad p_2=\frac{F_2}{a_0c_Z},$$
$$x_1=\frac{q_1}{a_0},\quad x_2=\frac{q_2}{a_0},\quad \vartheta=\frac{k_P}{a_0\omega_0^2\mu m_1},\quad \kappa=\frac{1}{\omega_0C_PR_P},\quad \theta=\frac{k_Pa_0}{C_P}.$$

The derived mathematical model is a formal basis for quantitative and qualitative model research within the field of assessing the efficiency of harvesting energy from vibrating mechanical devices. Model tests of the hybrid energy harvesting system were carried out assuming the physical parameters of the formulated phenomenological model, shown in Table 1.

Table 1. Geometric and physical parameters of the model

Name	Symbol	Value
Mass of a Duffing-type oscillator	m_1	*0.25 kg*
Loading mass of the cantilever beam	m_2	*0.02 kg*
Duffing-type oscillator losses	b_1	*0.35 Nsm^{-1}*
Cantilever beam losses	b_B	*0.02 Nsm^{-1}*

Losses in a system with quasizero stiffness	b_2	$0.28\ Nsm^{-1}$
Duffing-type oscillator mechanical characteristic coefficients	c_1	$144\ Nm^{-1}$
	c_2	$35 \cdot 10^{7}\ Nm^{-5}$
Equivalent stiffness of the quasizero stiffness system	c_Z	$36 \div 144\ Nm^{-1}$
Design dimension of the quasizero stiffness system	a_0	$0.03\ m$
Load resistance	R_O	$1.1\ M\Omega$
Equivalent capacity of the piezoelectric converter	C_P	$72\ nF$
Electromechanical constant of piezoelectric converter	k_P	$3.985 \cdot 10^{-5}\ N/V$

The dimensionless mathematical model and the adopted numerical data constitute the formal basis for conducting quantitative and qualitative numerical experiments.

3. Numerical calculations results

Examples of diagrams of the effective values of the voltage induced on the piezoelectric electrodes, for coexisting solutions, are presented in Fig.3. For each value of the dimensionless frequency, ω, 500 random initial conditions in a four-dimensional phase space were investigated. They were chosen within the range of the state variables, $x_i \in [-4,4]$, $\dot{x}_i \in [-4,4]$, and $i = 1,2$. Initial model studies, where initial conditions were selected to a lesser extent due to their variability, did not detect permanent 1T-period solutions characterized by the best energy harvesting efficiency. For all identified diagrams, the branches corresponding to zero initial conditions are presented in blue within Fig. 3.

Furthermore, diagrams of RMS voltage values were drawn with the assumption that the steady state occurs after 1000 periods of the excitation signal. This value was chosen to minimize the impact of transient processes which are subject to earlier or later extinction, depending on the solution. However, choosing a long lifetime of transient processes does not always guarantee their extinction because numerical artifacts are still visible, as shown in the cyan bands. Detailed model studies were carried out assuming the steady state occurs after 3000 periods of excitation. This showed that the periodic solutions with high periodicity are unstable and are attracted over time by low-energy orbits with a periodicity of 1T.

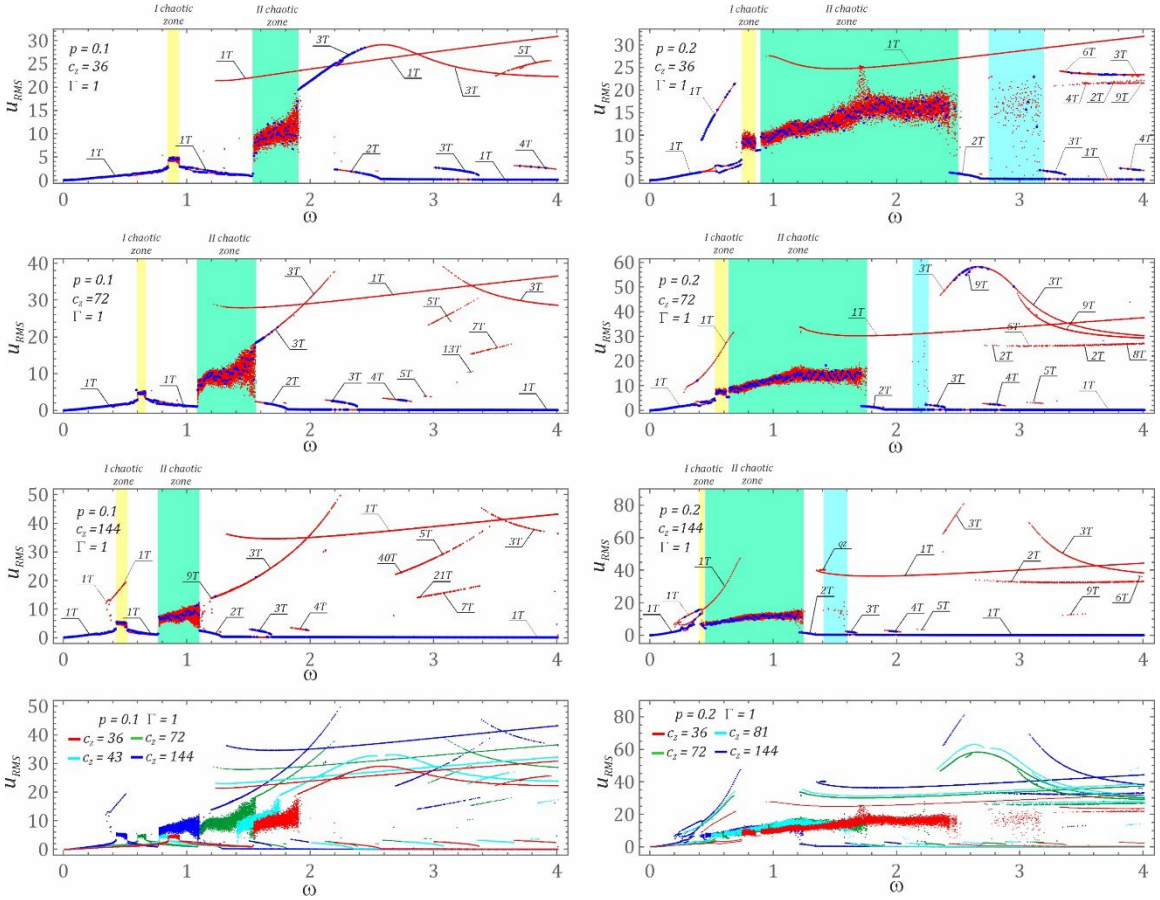

Fig. 3. Diagrams of RMS values of the induced voltage on piezoelectric electrodes, identified in relation to the deep wells of the potential barrier characterizing the Duffing-type oscillator. Blue trajectories correspond to zero initial conditions, other colors correspond to different values of c_z and p. Chaotic zones are highlighted in yellow and green.

Computer simulations indicate that there are two zones of chaotic solutions in the hybrid energy harvesting system, with the first being much narrower. An increase in the dimensionless amplitude of mechanical vibrations, p, affecting the system, causes an increase in the width of the chaotic response bands and a narrowing of the periodic response area between them, as shown in Fig. 3. However, the situation is the opposite in the case of increasing the equivalent stiffness, c_Z. A direct comparison of the diagrams shows that an increase in c_Z causes the branch to shift toward the low frequencies, ω. Simultaneously, an increase in the voltage induced on the piezoelectric electrodes is observed. In the low value range of $0.2 < \omega < 0.45$ ($p = 0.2$, $c_Z = 144$), periodic solutions with the periodicity of 1T appear, for which the orbits of the Duffing oscillator solutions circle both potential wells. This behavior is caused by the appearance of an additional branch of the 1T periodic solution. It is worth noting that at a certain value of c_Z, the branch representing the 3T-periodic solutions is broken. In the examples: $p = 0.1$, $c_Z = 36$; and $p = 0.2$, $c_Z = 72$, the vertices of the branches are within the zone, $\omega \in [2.4, 2.8]$. The 3T-period branch for $p = 0.1$ is broken when the equivalent stiffness of the system with quasizero stiffness is approximately $c_Z = 43$, shown via the cyan diagram.

Regarding the diagrams of the effective values for voltage induced on the piezoelectric electrodes ($p = 0.2$), the approximate equivalent stiffness was determined to be $c_Z = 81$, where the branches were broken. Regardless of the dimensionless amplitude of mechanical vibrations affecting the tested energy harvesting system, broken branches of 3T periodic solutions move in opposite directions. The left section moves towards the low values

of ω, while the right section moves towards the high values of ω. Most periodic solutions with a periodicity of 1T show a low energy harvesting efficiency of u_{RMS} <5., These solutions usually correspond to zero initial conditions and are located inside the potential well of the Duffing oscillator. The presence of two different solutions is visible with an increase in the equivalent stiffness of the quasizero stiffness system.

When the excitation frequency, ω, is located before the first zone of chaotic solutions, the vibrations of the cantilever beam, *I*, are much higher compared to the vibrations of the inertial element, *III*, shown in Fig. 4a. They are also larger compared to the vibration signal of the object, where the energy is obtained. Here, the system functions as a multiplier, and from a theoretical aspect, this property is favorable. However, the efficiency is too low to be an effective energy harvesting system. Within this band, and for low values of c_Z>36, the orbits of the 1T-period solutions coincide regardless of the operating points of the Duffing oscillator, which are in different potential wells. However, increasing the equivalent stiffness, c_Z, distorts the ellipsoidal phase trajectory of the Duffing system. This distortion becomes greater with increasing dimensionless amplitude of mechanical vibrations, which affect the tested energy harvesting system, shown in Fig. 4a. The phase trajectories of the system solutions with quasizero stiffness are plotted in a darkened color, while the corresponding orbits of the Duffing oscillator are in a brightened color. Poincaré cross-section points of the system with quasizero stiffness are distinguished by a black circle (Fig. 4).

An extremely different response is observed for higher values of ω. For these cases, the energy harvesting system functions as a vibro-isolator and applies to 1T-periodic solutions generating low voltages on the piezoelectric electrodes, as shown in Fig. 4b. There is no orbit deformation of the system with quasizero stiffness because there is a very strong vibration isolation in the system. For higher values of the dimensionless excitation frequency, ω> 2, the effective induced voltage on the piezoelectric electrodes is near zero. The orbits of the Duffing oscillator solutions do not leave the potential well, while solutions with higher periodicity for the system with quasizero stiffness are excited. Based on the numerical experiments carried out, it is possible to conclude that we have effective energy harvesting when the trajectory of the Duffing oscillator runs around the potential wells.

a)

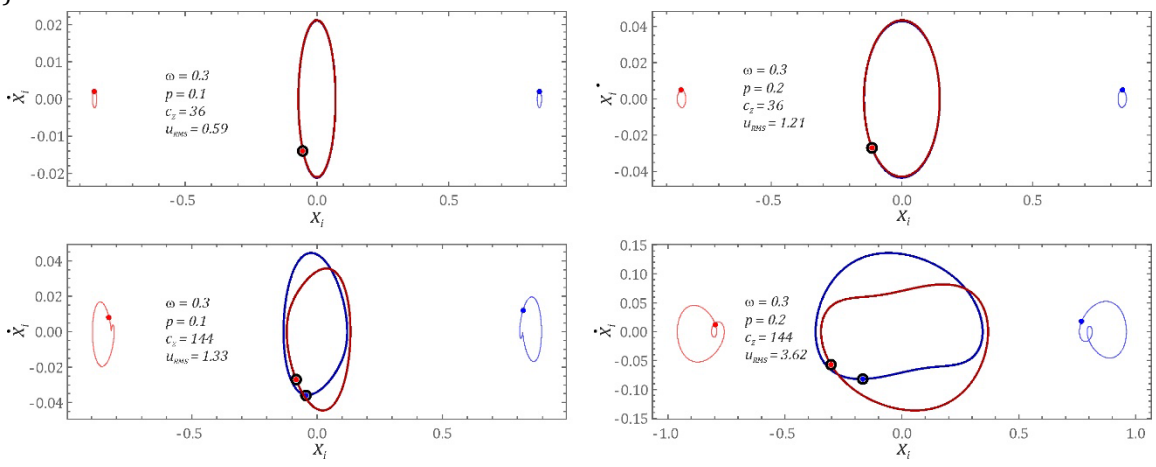

b)

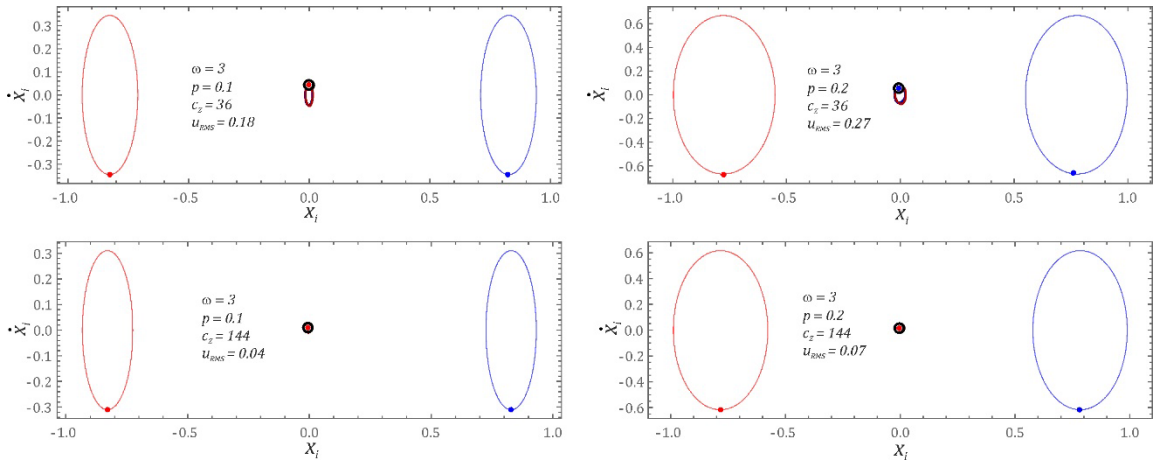

Fig. 4. Influence of the equivalent stiffness of an oscillator with quasizero stiffness on the shape of 1T-periodic orbits. in the range of: a) low frequencies, b) high frequencies

Diagrams of RMS voltage values induced on the piezoelectric electrodes are shown in Fig. 5. They show the effect of the potential barrier well depth on the solutions and the geometric structure of the branches. If the potential well depth decreases, then a narrowing of the zones of chaotic solutions is observed. Similar to the graphs presented in Fig. 3, an increase in the equivalent stiffness, c_Z, improves the efficiency of energy harvesting from vibrating devices. Regarding the tested c_Z weights, the "breaking" of the solution branches with a periodicity of 3T takes place for lower values of c_Z. For shallower wells, branches representing quasi-periodic, *QZ,* solutions are excited in the system. In the hybrid energy harvesting system, there are branches representing even and odd periodic solutions. Regardless of the excitation amplitude, *p,* and the depth of the Duffing oscillator's potential barrier well, 1T-periodic solutions with low energy efficiency dominate in the bands before the first chaotic solution zone. For low values of the excitation amplitude, *p*, these solutions correspond to zero initial conditions. The focus is on solutions with higher periodicity when the dimensionless excitation frequency, ω, leaves the second chaotic zone.

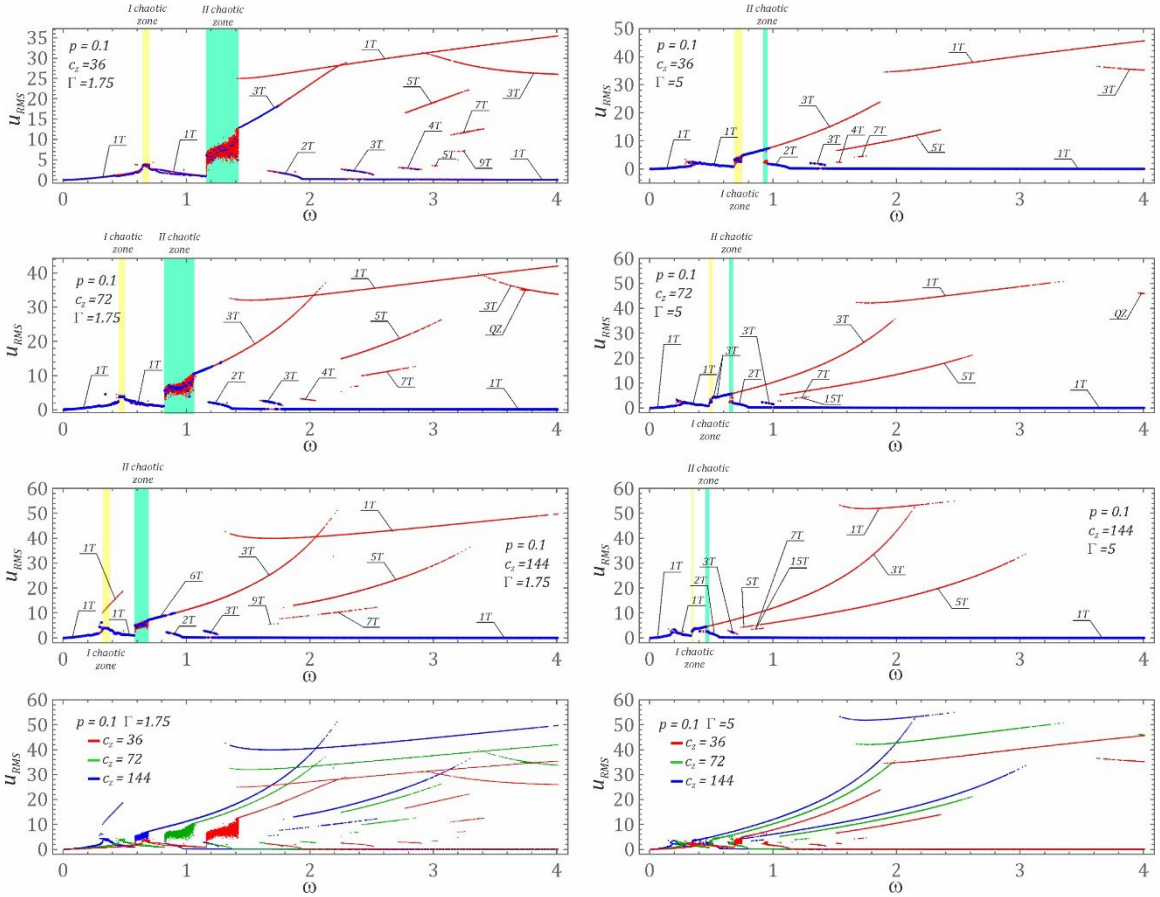

Fig. 5. Diagrams of the effective voltage induced on piezoelectric electrodes, which were identified for the shallow and transient well depths of the potential barrier Γ, characterizing the Duffing oscillator. Blue trajectories correspond to zero initial conditions, while other colors correspond to different values of c_z and Γ. Chaotic zones are highlighted in yellow and green.

The results of numerical experiments above indicate that effective energy harvesting from mechanically vibrating devices takes place for high equivalent stiffness, *cz*, values. The impact of the dimensionless excitation amplitude, *p,* and the depth, Γ, of the Duffing oscillator's potential barrier on the structure of the diagram was compared in Fig. 6.

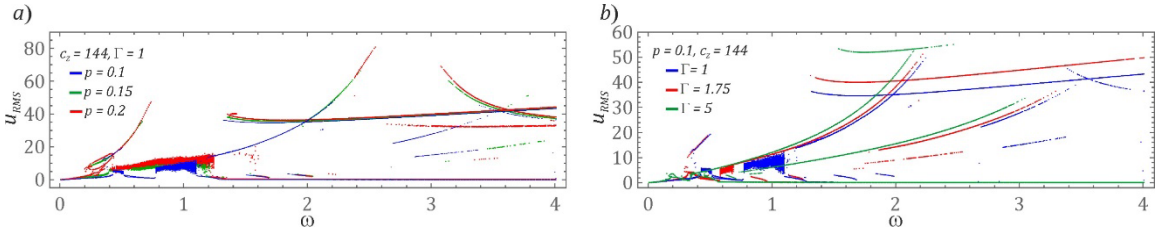

Fig. 6. The results of the model tests showing a) the influence of the dimensionless amplitude, *p,* b) the Duffing oscillator's potential barrier well depth, Γ. Colors correspond to different values of *p* and Γ.

The results in Fig. 6a show that, irrespective of the dimensionless amplitude, *p*, branches with a periodicity of 1T running almost parallel to the frequency axis, ω, do not change their position. For these cases the increase in *p* causes the extension of the left section of the 3T-periodic branch. However, Fig. 6b shows that as the depth of the Duffing

oscillator well decreases, the slope of the diagram branches increases. Graphs of the coexisting periodic solution orbits are not presented here. They will be presented later when assessing the disturbing impulse for the possibility of a phase trajectory correction.

3.1. Single impulse correction of the solution

The basis for the numerical experiments included in this section is the 'Impulse Excitation Diagram' (IED). Generally, the algorithm is drawn based on the identified Poincaré points, which are compared with the points of coexisting solutions. Here, during computer simulations, it was assumed *a priori* that the disturbing impulse is initiated the moment the hybrid energy harvesting system is in steady-state motion. From the beginning of the computer simulation, $\tau = 0$, until the dimensionless time reaches τ_0, only the mechanical vibrations of the object act on the tested system. In the steady state condition, when the excited transient processes are extinguished, there is a stable solution that corresponds to zero initial conditions $x_1(0) = 0, \dot{x}_1(0) = 0, x_2(0) = 0, \dot{x}_2(0) = 0, u(0) = 0$. Only at τ_0 is the disturbing impulse initiated. The additional dynamic action causes the operating point to be thrown out of the stable orbit. During the visualization of the solution correction, all resulting orbits (corrected) were drawn in red. The phase trajectory corresponding to the transition processes is shown in gray. Over time, these trajectories tend to be one of the permanent periodic or chaotic solutions. The targeted orbit is highlighted in blue.

To illustrate the behavior of phase flow during the excitation impulse, its fragments have been distinguished by dashed curves in black and brown. Poincaré points of coexisting solutions are mapped with markers where the colors correspond to the colors of the permanent responses of the system. The moments in which the impulse initiation takes place are marked with black circles. The same process was applied to the moment of stopping the impulse and the appropriate point on the phase plane was marked with a white marker. For model tests results presented in Figs 7 and 8, IED diagrams were identified with respect to time windows where the width is equal to one excitation signal period.

For the IED diagrams, the time series of mechanical vibrations (navy blue) and the excitation impulse (blue and dark gray) are plotted. The colors of the orbits of the coexisting periodic solutions are directly correlated with the colors of the IED diagram – it shows the moments of time in which it is possible to achieve a solution of a given color. The sum of the time moments of a given color versus the total time on the IED defines the probability of achieving a given solution. Only the bands, corresponding to the initiation of the solution's orbits in orange, are highlighted in yellow. This substitution ensured an appropriate contrast for the readability of the IED diagram. This approach was adopted for the presentation of all numerical experiment results included in the paper.

Theoretically, the solution orbit correction can be achieved in three ways including via a direct disturbance of the vibration signal. This approach was considered in the publication by Margielewicz et al. [24] and is not investigated in this paper. The other two options are direct force impulses influencing the inertial elements of the Duffing oscillator, p_1, and the system with quasizero stiffness, p_2. During the numerical experiments, the amplitudes of the excitation impulses influencing individual oscillators were assumed to be the same. The times at which the impulse is initiated, τ_0, were calculated for 700 points in the time window. For each band, the probability of reaching the individual orbits was estimated based on the IED.

The dynamics of the system are of little interest for the low-value band of the dimensionless excitation frequency, ω, which is limited by the first zone of chaotic solutions.

Similarly, this applies to the small values of the dimensionless amplitude, p <0.2, of mechanical vibrations affecting the hybrid energy harvesting system. This is due to the coexistence of solutions with Duffing oscillator orbits located inside the potential well. For such orbits, correcting the solution is not effective because the initiated impulse will cause the solution to jump from one well to the other without a noticeable qualitative change in voltage induced on the piezoelectric electrodes. Large orbits in these zones were identified for p = 0.2 and c_Z = 144 for the system with quasizero stiffness, shown in Fig. 3.

The coexistence of the orbits covering both wells of the Duffing oscillator is shown in Fig. 7a. There are three permanent periodic solutions with a periodicity of 1T. The energy harvesting efficiency in two of them is low because their orbits are located inside one of the potential wells. Therefore, the effective voltage induced on the piezoelectric electrodes reaches a value of circa 2.6V. The orbit in orange corresponds to zero initial conditions.

If the impulse acts on the inertial element of the Duffing oscillator, then the bands represented in yellow dominate in the IED diagram, shown in Fig. 7b. Initiating an impulse within this band and allowing the transient processes to decay, the phase flow is attracted to the targeted orbit. However, in the case of an external impulse with an amplitude of $p_1 = 1.5$ (20.25N excitation force) and a width of $\tau_1 = 0.25$, only 3% of the identified moments, τ_0, achieve the orbit with the highest energy harvesting efficiency, shown in red. The diagram showing the time moments of the impulse initiation affecting the oscillator with quasizero stiffness and the solution correcting phase trajectory is shown in Figure 7f. Both diagrams are dominated by the yellow bands leading to the orange orbit in Fig. 7b, which corresponds to zero initial conditions. Additionally, the red bands leading to the large orbit are very narrow. For the impulse influence on the Duffing oscillator, $p_2 = 18.75$, corresponding to a force of 20.25N, the probability of obtaining a solution given by a large orbit is circa 3%, as shown in Fig. 7b. However, when impulse acts on an oscillator with quasizero stiffness, the probability is circa 4.86%, shown in Fig. 7f.

The numerical experiments show that increasing the amplitude of the disturbing impulse has a beneficial effect on the structure of the diagram. This is due to the width of the bands increasing, which is synonymous with a greater probability of achieving a large orbit. For example, doubling the p_i impulse amplitude increases the probability of reaching a large orbit by a factor of ten, as shown in Fig. 7d and Fig. 7e. However, this takes place when the disturbing impulse affects the Duffing-type oscillator. When an impulse with the same characteristics is applied to a system with quasizero stiffness, there is over a fourteen-fold increase in the bandwidth, leading to a large orbit, shown in Fig. 7h and Fig. 7i.

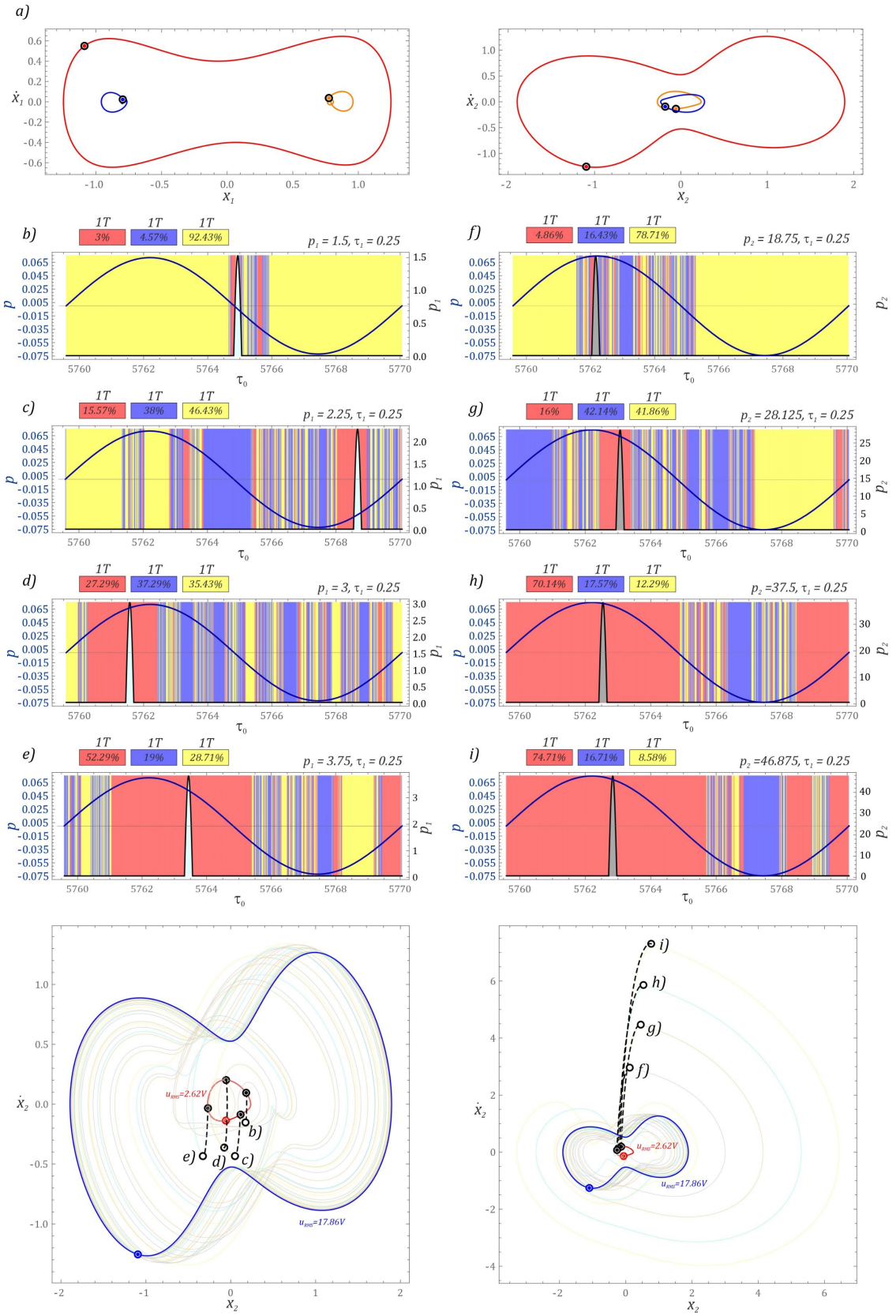

Fig. 7. The impulse amplitude influence on the structure of the impulse excitation diagram. The orbits for the disturbing impulse amplitudes are distinguished in colors. The time and amplitude of the impulse, the probability of achieving a solution, and the moment of impulse initiation are presented: p_2 – impulse amplitude affecting quasizero system, p_1 –impulse amplitude affecting Duffing oscillator. Time series of mechanical vibrations are in navy blue and the excitation impulse is in blue and dark gray. τ_1 is the impulse duration.

Analogous tests were performed regarding the parameter τ_1, defining the impulse width. The computer simulation results indicate that the impulse width has a small influence on the broadening of the IED diagram bands, shown in Fig. 8.

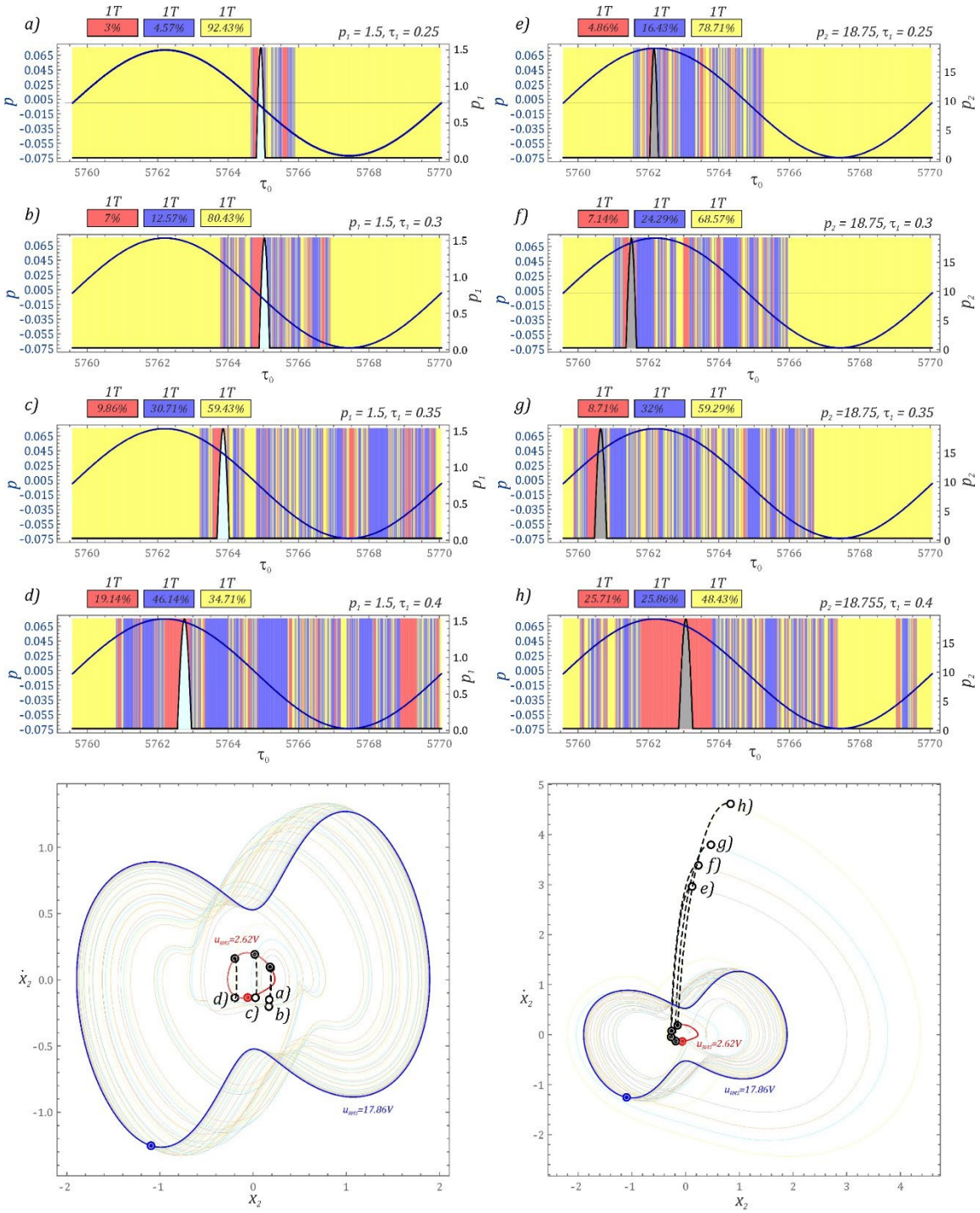

Fig. 8. Impulse width effect on the structure of an IED diagram. The trajectories for different impulse widths, τ_1, (impulse duration time) are distinguished by colors. The time and amplitude of the impulse, the probability of achieving a solution, and the moment of impulse initiation are presented: p_2 – impulse amplitude affecting quasizero system, p_1 – impulse amplitude affecting Duffing oscillator. Time series of mechanical vibrations are in navy blue and the excitation impulse is in blue and dark gray.

The numerical experiment results show the possibility of defining the impulse characteristics to achieve a given solution.

3.2. Technical capabilities of solution corrections

The numerical experiments results presented so far explore the coexisting solutions with orbits that are within proximity. However, when dealing with several coexisting orbits where distances between the output and targeted orbits are large, then for inertial elements it is necessary to initiate a large amplitude impulse. Technically, the amplitude of the impulse is limited, therefore numerical experiments were carried out where the system was influenced by characteristics of the disturbing load. The main aim of this research was to reduce the amplitude of the impulses. However, at very large distances between the output and the targeted solutions, generating a sufficiently large amplitude may turn out to be impossible.

Results are plotted in Fig. 9, showing cases where the disturbance affects a Duffing oscillator. These conclusions are made due to the legibility of the charts. For impulse interactions in a system with quasizero stiffness, the disrupted trajectory is "launched" into further regions of the phase space. Additionally, the same values were assumed for the amplitudes, p_1, and widths, τ_1, of the impulses. The time delay, τ_2, measured between the end of the first impulse and the beginning of the second impulse, was assumed to be twice the impulse width, τ_1.

Appropriate model studies were carried out relating to five coexisting stable periodic solutions. Three of them are 1T periodic solutions, while the other two have a 5T and 7T periodicity. For orbits observed in the phase plane of the Duffing-type oscillator, two 1T-periodic responses are located inside the potential well and have near-zero energy harvesting capacity. This low efficiency of energy recovery is directly related to the high value of the dimensionless excitation frequency, ω. Due to high values of ω, the system functions as a vibration isolator.

The 1T-periodic solution highlighted in red in Fig. 9a shows the best energy harvesting efficiency, $u_{RMS} \approx 35.4V$. The 5T and 7T periodic responses are in the zone between the large and small orbits. Based on the identified impulse excitation diagrams, it can be concluded that the 5T and 7T periodic solutions have a relatively low probability of achieving a similar solution. Fig. 9c shows that the probability of achieving the 5T-period solution reaches the level of 11.14%. For the 7T-periodic solution, this probability is smaller, with a maximum value of 3.57%.

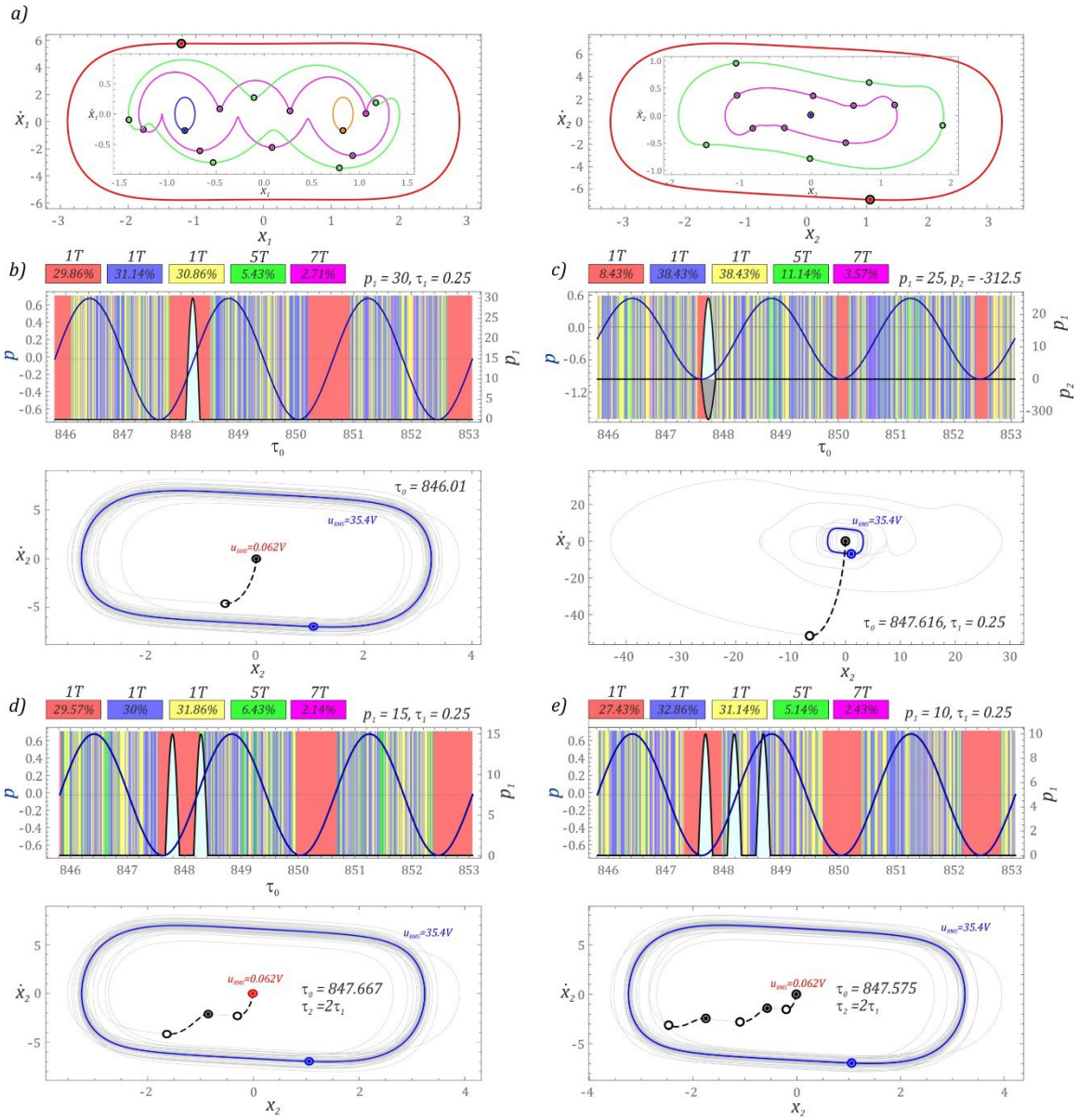

Fig. 9. Various characteristics of the impulses. a) one impulse affecting Duffing oscillator, b) two impulses affecting Duffing oscillator and quasizero system, c) two impulses in sequence affecting Duffing oscillator, d) three impulses in sequence affecting Duffing oscillator. τ_2 is the time delay measured between the end of the first impulse and the beginning of the second impulse. Model test results for: $p = 0.1$, $\omega = 2.6$, $\Gamma = 1.75$, and $c_z = 72$

The impulse excitation diagrams shown in Fig. 9 illustrate the influence of the external dynamic interaction on the ability to reach the targeted orbit. When designing a system correcting the orbit of the solution, it is important to know that the amplitude of the disturbing impulse has a finite value. As it increases, the necessary energy to initiate an impulse also increases. The term "necessary energy" means the total force that must be applied to achieve the desired orbit. Considering the limited energy efficiency of the impulse-initiating system, numerical experiments were carried out while various dynamic characteristics disturbing the output orbit were tested.

When the system is affected by a single impulse, the targeted solution can be achieved when the impulse width, $\tau_1 = 0.25$, and its amplitude, p_1, reaches a dimensionless value of approximately 30, which corresponds to circa 810N. Smaller amplitudes of the disturbing impulse make it impossible to obtain a solution with the best energy efficiency. Based on

the identified diagram of excitations in Fig. 9b, it is possible to estimate the probability of achieving solutions. Initiating a large load of approximately 800N, will likely not be achievable from an engineering point of view by using a small forcing system. Therefore, the orbit was disturbed by a load acting simultaneously on Duffing oscillator and quasizero stiffness system, shown in Fig. 9c. However, in principle a satisfactory result cannot be achieved either because the actual amplitude value of each impulse is 675N. Despite the probability of reducing the amplitude of disturbing impulses by approximately 20%, the probability of achieving the most energy-efficient solution has been reduced more than three times. With this characteristic of a solution disturbance, the impulses acting on the Duffing-type oscillator, as well as the quasizero stiffness system, should have opposite directions. For impulse vectors with the same direction, much worse effects of orbit correction are obtained relating to the disturbance, with a single impulse affecting any oscillator.

Much better results are obtained if the Duffing-type oscillator is influenced by a sequence consisting of two impulses. Here, the actual amplitude of the impulses is limited to 405N, which is equivalent to its two-fold limitation. The probability of reaching the orbit with the best energy harvesting efficiency is comparable at 29.57%, shown in Fig. 9d.

Fig.9b shows that for the third impulse in the disturbing sequence the real values of the impulse amplitudes were three times smaller and circa 270N. Therefore, the probability of reaching a large orbit did not change significantly. The results of the model tests show that the most effective method of correcting the solution is influencing the inertial elements of the energy harvesting system with a series of excitation impulses. The numerical experiment results show that the total force of a single impulse is equal to the sum of individual impulses that should be allocated to change the solution regarding impulse sequences. This value is the same as for interactions with a single impulse, however, the impulse-initiating system may be much smaller which will be a technological advantage.

3.3. Coexistence of high-energy and low-energy orbits

For the coexistence of high and low orbits, the correction of the solution, with minimal force initiating disturbing impulses, is possible through a series of impulses. Considering low orbits, the effective voltage induced on the piezoelectric electrodes is u_{RMS} <5V, while for high and very high orbits it is u_{RMS}>20V. At this point, the boundary effective voltages are a subjective assessment of the authors. This paper copes with solutions in almost every identified diagram of coexisting solutions. Correcting the response for these solutions via the impulse sequence is reasonable as the amplitude of a single impulse may turn out to be physically unrealistic. However, for assessing the applied strategy of modifying the solution orbit, the results of computer simulations show that the IED identified for a single impulse is also included. The results of the numerical experiments are presented in the graphs shown in Fig. 10.

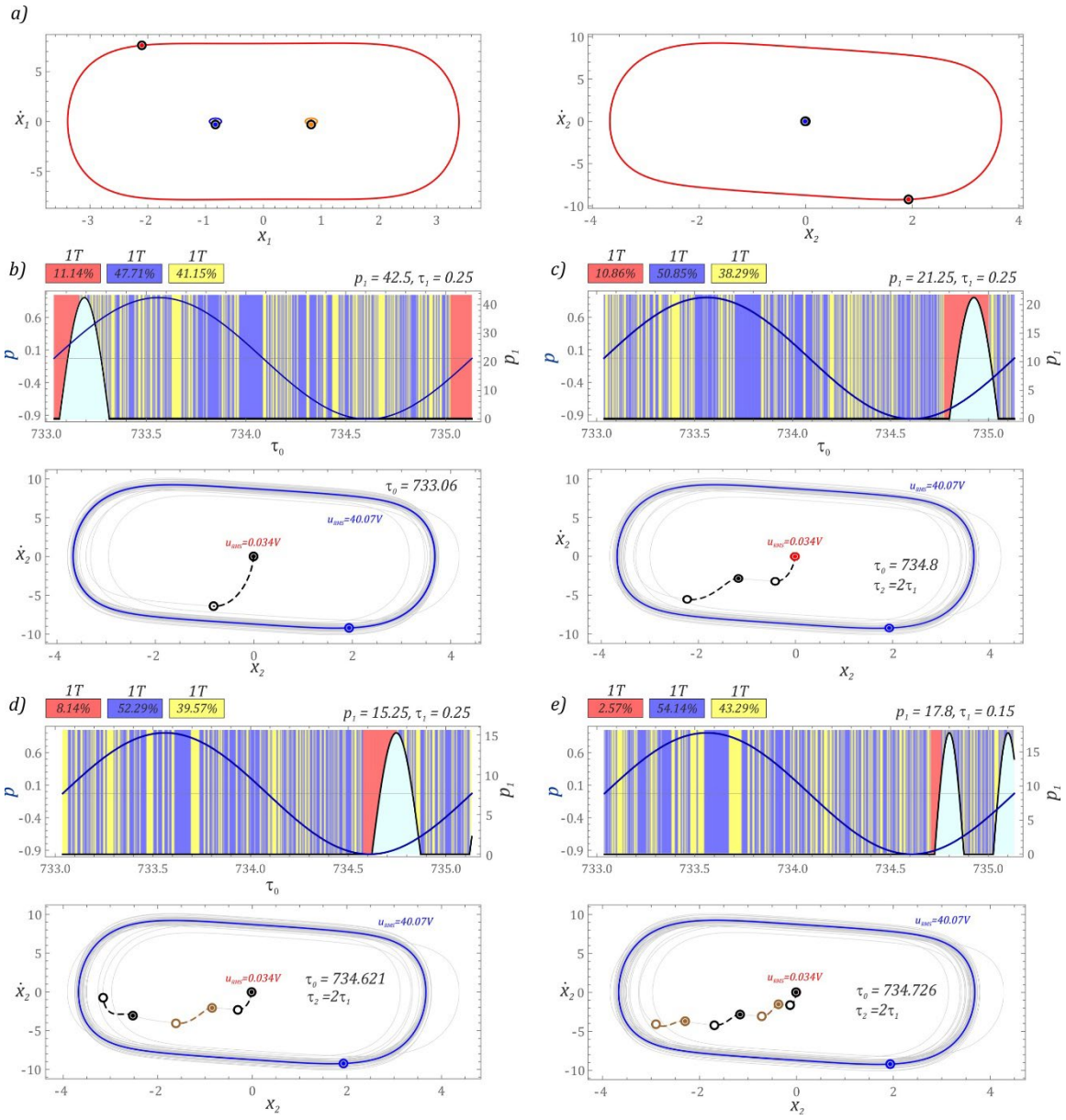

Fig. 10. Various characteristics of the impulses sequences for the coexistence of high and low orbits: b) one impulse, c) two impulses, d) three impulses, e) four impulses. Model test results for $p = 0.1$, $\omega = 3$, $\Gamma = 5$, and $c_Z = 36$

If the energy harvesting system with shallow potential barrier wells, $\Gamma = 5$, is affected by mechanical vibrations with an amplitude of $p = 0.1$ and a frequency of $\omega = 3$, then three coexisting solutions with the periodicity of 1T are possible. Two of them are located inside the Duffing oscillator's potential barrier well, shown in Fig. 10a. These solutions are characterized by a near-zero efficiency of harvesting energy ($u_{RMS} \approx 0.034$V). However, one solution located in the left well is the basic solution, which is a solution that corresponds to zero initial conditions. The third solution is characterized by the highest energy recovery efficiency given by a large orbit, where a voltage is induced on the piezoelectric electrodes with an effective value of $u_{RMS} \approx 40$V. The orbit correction via a single impulse can be achieved if the dimensionless amplitude of the p_1 impulse reaches a value of circa 42.5 (574N). With a given characteristic of the impulse, the probability of achieving the desired solution is circa 11.14%, shown in Fig. 10b. The amplitude of a single impulse is smaller than it was in the example presented in Fig. 10b. In this example, the distance between

the initial orbit and the target orbit is greater, yet the amplitude of the impulse is smaller. This is due to the value of the impulse amplitude being mainly determined by the equivalent stiffness of the system with quasizero stiffness.

A similar probability of 10.86% was recorded when the initial orbit was influenced by a sequence of two impulses of the same amplitude and width, shown in Fig. 10c. For this diagram, only one of them is visible, while the other is outside the scope of identification. The lack of a second impulse in the diagram is mainly due to the depiction of the moments of time leading to the other two solutions, and the location of the impulse initiation band located in the final range. Similar findings are made for the interaction with sequences consisting of three and four impulses. The initiation of two impulses on the Duffing oscillator made it possible to limit the amplitude of the impulses to the level of p_1 = 21.25, which corresponds to circa 287N. The analysis of the trajectory during the impulses shows that as they move away from the beginning of the coordinate system of the phase plane, the trajectories are deformed. This is caused by the areas of attraction near where the impulses stop. Along with increasing the number of impulses, it is possible to limit their amplitudes, however, this could reduce the probability of reaching the set target orbit. For three impulses, this probability reaches 8.14%, with a dimensionless amplitude of p_1 = 15.25, which corresponds to circa 206N, as shown in Fig. 10d.

The results of model studies presented so far suggest that the only panacea for correcting the solution in the coexistence of large and small orbits is to initiate sequences composed of multiple impulses. However, this was shown to be incorrect. In the example presented in Fig. 10e, the sequence of four impulses with a width of τ_1 = 0.25, and a delay of $\tau_2 = 2\,\tau_1$, did not provide satisfactory results. Due to a larger number of impulses, a situation may arise where the targeted trajectory is reached by one of the preceding impulses and each following impulse will knock the target orbit out of its steady state. Therefore, there are no bands on the IED leading to the target orbit. In these cases, both the impulse width, τ_1, and the delay, τ_2, can be reduced. Influencing the energy harvesting system through a series of four impulses provided satisfactory results. However, it was shown that it was necessary to reduce τ_1 by a factor of circa 2. With these impulse sequence characteristics, the probability of correcting the solution was approximately 2.57%.

Technically, the examples in the graphs shown in Fig. 10d and Fig. 10e show that the orbits corrected via a series of three and four impulses are pointless. This is due to the total energy required to correct the orbit being greater than the energy required to generate a single impulse. However, it is possible to further limit the amplitude of the impulses. Nevertheless, the consequences of this action are an increasingly narrower band of the desired orbit and a lower probability of successfully correcting the initial solution.

3.4. Coexistence of chaotic and periodic solutions

In nonlinear dynamical systems, it is common to have two coexisting chaotic and periodic solutions with a periodicity of 1T, shown in Fig. 11a. The periodic solution is characterized by a higher energy harvesting efficiency because the effective voltage on the piezoelectric electrodes is observed and reaches $u_{RMS} \approx 30.42$V. The zero initial conditions corresponding to the equilibrium position led to a chaotic solution with an energy harvesting efficiency almost twice as low as $u_{RMS} \approx 30.42$V, relating to the periodic response.

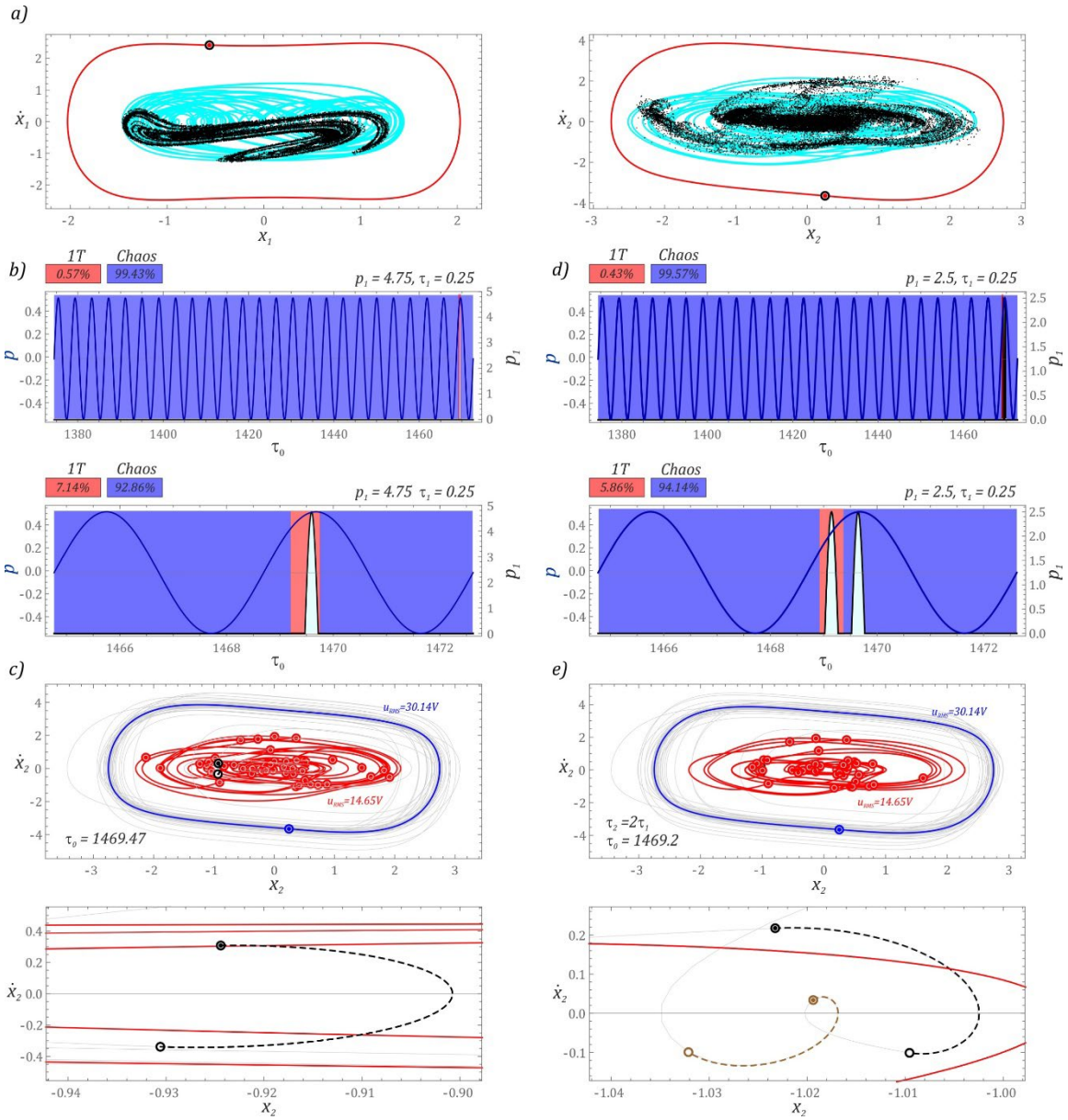

Fig. 11. Various characteristics of the impulses for the coexistence of chaotic and periodic solutions. Model test results for $p = 0.2$, $\omega = 1.6$, $\Gamma = 1$, and $c_Z = 72$

The identified IED diagrams were plotted for the Duffing-type oscillator being affected by an external dynamic excitation impulse of the lowest force required to enable the target orbit to be reached. Therefore, the probabilities of achieving the desired solution are less than 0.6%, as shown in Fig. 11b and Fig. 11c. For a disturbance with a single impulse, or a sequence of impulses, the probability increases over ten-fold. This comes from the algorithm calculating the excitation diagrams because the probability of achieving the solution is estimated via the number of moments, τ_0, examined while plotting the diagrams. However, optimizing the impulse characteristics due to its minimum amplitude is not advisable. This is due to the impulse characteristic being determined by the dynamics of the impulse-initiating system.

The initiating system should be characterized by a slight inertia and the electronics responsible for its control are important. With two coexisting solutions, where one is chaotic, excitation impulses should be initiated at the time τ_0, when the distance between the

chaotic trajectory and the target orbit is the minimum. These cases are not included because they occur at higher dimensionless amplitudes of the disturbing impulses. However, this hypothesis is not confirmed by the obtained results of computer simulations. This is the case with a single disturbance in Fig. 11c and a sequence of two impulses from Fig. 11e. As seen in the examples already tested, shown in Fig. 11d, increasing the number of disturbing impulses enables their amplitude to be nearly half. However, this action is futile since the total amount of energy devoted to correcting the solution is greater than the energy used to initiate a single impulse, as shown in Fig. 11b. As with the impulse excitation diagrams, enlargements of the phase plane are presented to visualize the trajectory during the impulse interaction.

3.5. A step-by-step method of correcting solutions

This section presents an alternative method showing it is possible to achieve the highest energy efficiency solution. This method corrects the target orbit in several stages. At each stage, an orbit with a higher energy efficiency should be achieved. Theoretically, the total energy devoted to initiating impulses should be smaller than correcting the solution with a single impulse.

Detailed modeling studies were performed for the coexistence of six solutions. Three of them are characterized by 1T-periodic orbits, but for one of them, shown in red in Fig. 12a, the effective voltage induced on the piezoelectric electrodes reaches the level of $u_{RMS} \approx 52.2$V. The solutions located inside the Duffing oscillator well show close to no energy harvesting efficiency. Based on the analysis of the orbits, it can be concluded that the periodicity of the solutions decreases as the voltage induced on the piezoelectric electrodes increases. Of the orbits revolving around both potential wells of the Duffing oscillator, the lowest energy harvesting efficiency is found in two 5T-periodic solutions of $u_{RMS} \approx 13.15$V. The 3T-periodic solution shows a much higher efficiency because the RMS voltage on the piezoelectric electrodes reaches $u_{RMS} \approx 32.84$V.

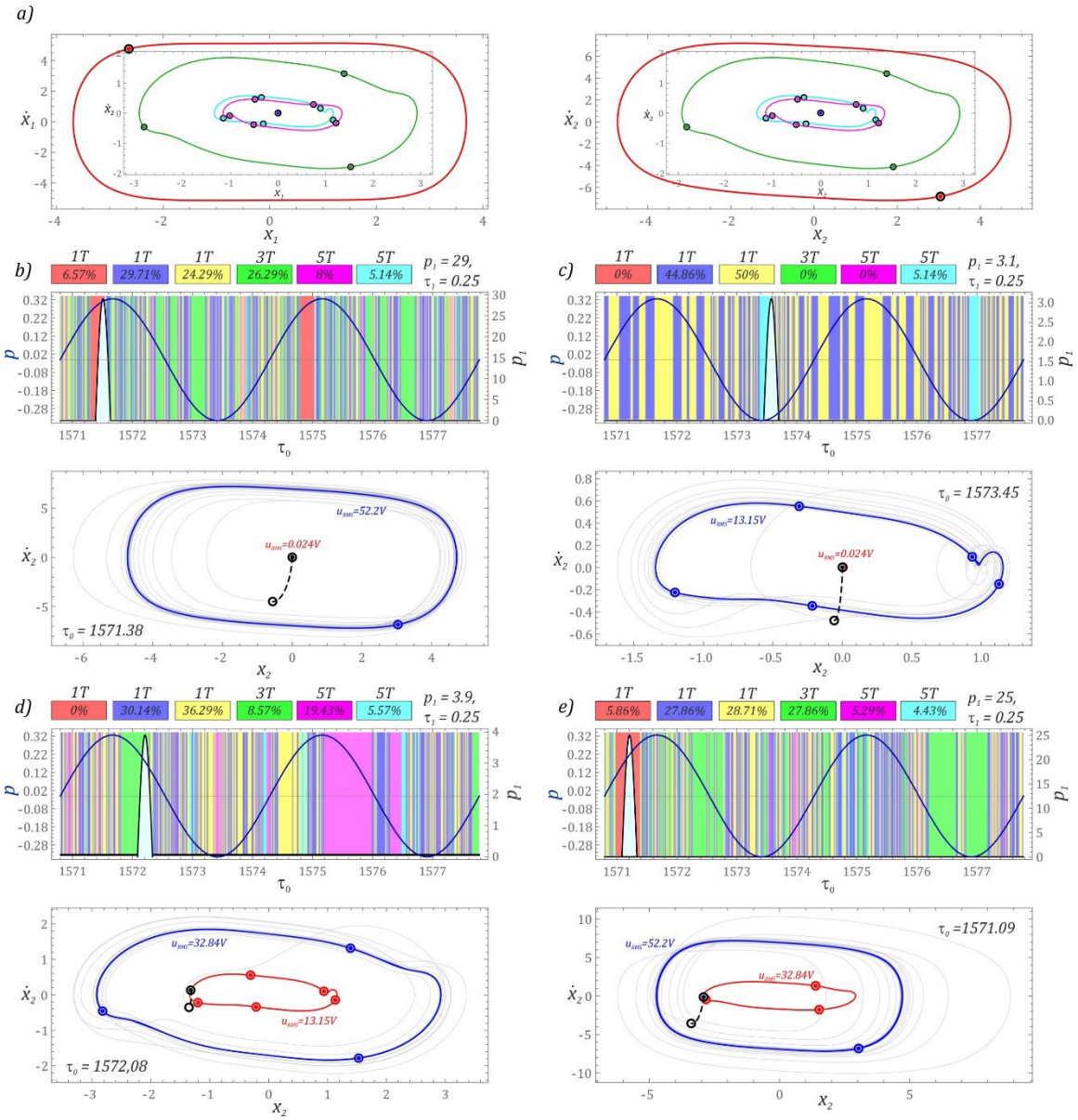

Fig. 12. A step-by-step method of correcting solutions: a) high-energy orbit in red, b) one impulse to high-energy orbit, c), d), e) three impulses in the step-by-step method. Model test results for the case were $p = 0.1$, $\omega = 1.8$, $\Gamma = 5$, and $c_Z = 144$

The total energy required to reach the target orbit by the step-by-step method was compared to directly correcting the solution, shown in Fig. 12b. For the direct method, it is necessary to initiate an impulse with a dimensionless amplitude of p_1 = 29, which is circa 1560N. In the step-by-step approach, the first step in "reaching" the desired solution is being able to achieve one of the two 5T-periodic solutions. The choice of one depends on the structure of the band distribution in the impulse excitation diagram. In Fig. 12c, when a single impulse with a dimensionless amplitude of p_1 = 3.1 is initiated on the Duffing oscillator, only one of the solutions with a periodicity of 5T is achievable with a probability of 4.43%. In the second stage, a jump to the orbit of the 3T-periodic solution is made. Here, the minimum amplitude of a single disturbing impulse is p_1 = 3.9, shown in Fig. 12d.

The similar values of the impulse amplitudes necessary to correct the orbit in both stages can be explained by the similar difference in the effective voltages of the initial and target solutions. The results of computer simulations obtained in both stages suggest that

the large 1T-periodic orbit will be reached at a similar impulse amplitude. However, this does not take place because the simulations indicate that near the 3T-periodic orbit there are areas of attraction leading to other coexisting solutions. Leaving the orbit requires initiating an impulse with a dimensionless amplitude of $p_1 = 25$, as shown in Fig. 12e. This excessive value should be attributed to the strong influence of the vector field, which causes the trajectory to stretch over the duration of the impulse. The results of computer simulations show that achieving the orbit with the highest energy generation efficiency should be obtained through a single impulse.

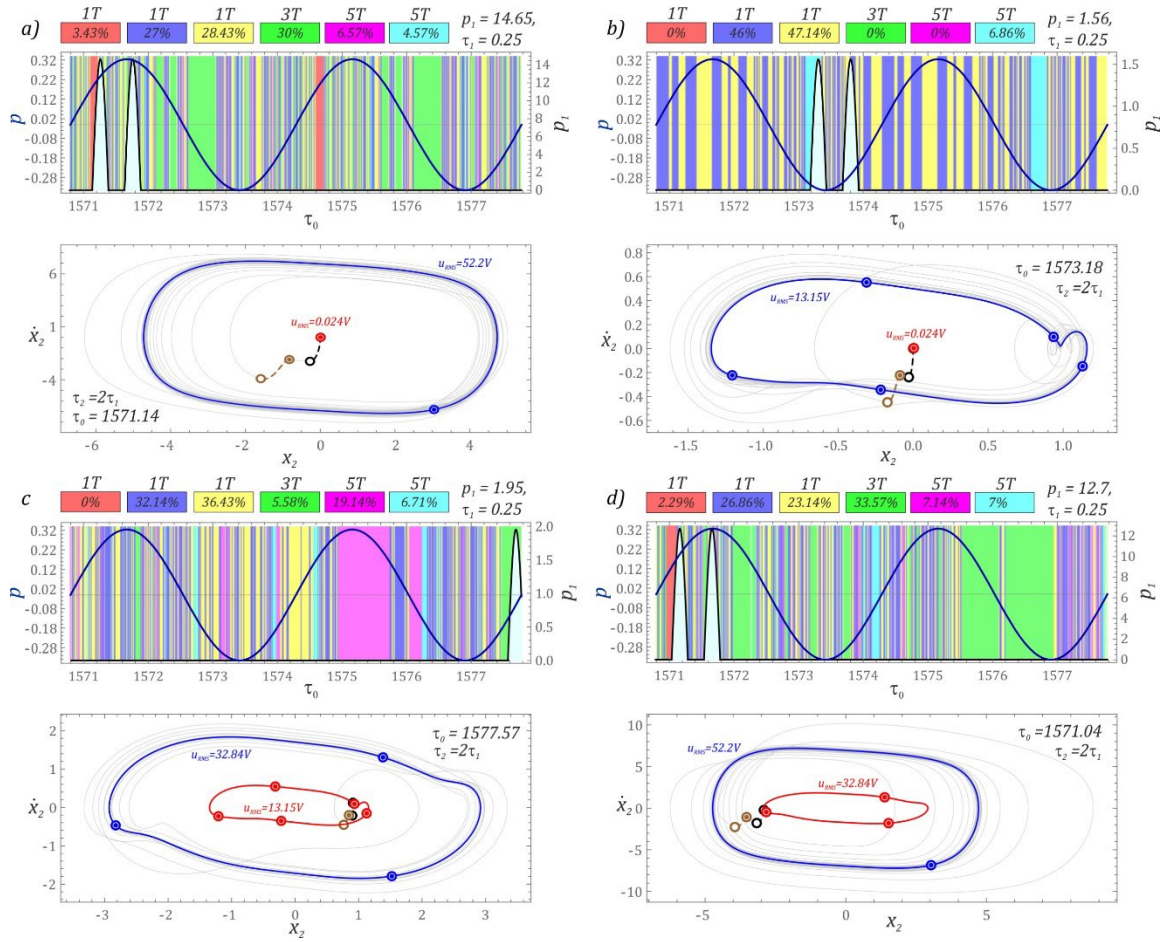

Fig. 13. A step-by-step method of correcting solutions with a sequence of two impulses. Model test results for $p = 0.1$, $\omega = 1.8$, $\Gamma = 5$, and $c_Z = 144$

Similar tests were carried out where the correction of the solution is performed with the step-by-step method and a sequence of two impulses, as shown in Fig. 13. Here it is necessary to increase the amplitude by many factors in the third stage of correcting the solution. Fig. 13 shows that the energy needed for changing the orbit of the solution is at a similar level to the interaction with a single impulse.

4. Summary and final conclusions

Based on the model tests performed, it is possible to formulate the following conclusions:

- If the system is affected by mechanical vibrations with an amplitude of $p \leq 0.1$, then with respect to the energy harvesting efficiency, the equivalent stiffness of the oscillator with quasizero stiffness should assume large values. For $p \geq 0.1$, it is advisable to increase the equivalent stiffness.
- The probability of reaching the desired orbit can be increased by using a larger amplitude and duration of disturbing impulses.
- The amplitude of the impulses disturbing the stable orbit is determined by the equivalent stiffness of the oscillator with quasizero stiffness. Therefore, when designing the energy harvesting system, it is necessary to ensure the lowest possible value of the c_Z parameter.
- Not all solutions with the highest efficiency of energy harvesting can be achieved due to the technical limitations of the system initiating the impulse.
- The step-by-step method is a strong alternative to the typical methods based on one or more impulses. It is important to choose the time of the impulses and the time between them. Optimization of these parameters enables a more effective orbit change with the use of a smaller impulse excitation system. The amount of energy required to change the orbit is comparable to a single-impulse excitation system. A major advantage is a much smaller construction for the step-by-step system.

References

[1] Johnson TJ, Charnegie D, Clark WW, Buric M, Kusic G, Johnson TJ, et al. Energy harvesting from mechanical vibrations using piezoelectric cantilever beams. SPIE 2006;6169:81–92. https://doi.org/10.1117/12.659466.

[2] Sodano HA, Park G, Inman DJ. Estimation of Electric Charge Output for Piezoelectric Energy Harvesting. Strain 2004;40:49–58. https://doi.org/10.1111/J.1475-1305.2004.00120.X.

[3] Erturk A, Hoffmann J, Inman DJ. A piezomagnetoelastic structure for broadband vibration energy harvesting. Appl Phys Lett 2009;94:254102. https://doi.org/10.1063/1.3159815.

[4] Erturk A, Inman DJ. Piezoelectric Energy Harvesting. Chichester, UK: John Wiley and Sons; 2011. https://doi.org/10.1002/9781119991151.

[5] Zhu D, Tudor MJ, Beeby SP. Strategies for increasing the operating frequency range of vibration energy harvesters: a review. Meas Sci Technol 2009;21:022001. https://doi.org/10.1088/0957-0233/21/2/022001.

[6] Kumar A, Balpande SS, Anjankar SC. Electromagnetic Energy Harvester for Low Frequency Vibrations Using MEMS. Procedia Comput. Sci., vol. 79, Elsevier B.V.; 2016, p. 785–92. https://doi.org/10.1016/j.procs.2016.03.104.

[7] Aouali K, Kacem N, Bouhaddi N, Mrabet E, Haddar M. Efficient broadband vibration energy harvesting based on tuned non-linearity and energy localization. Smart Mater Struct 2020;29:10LT01. https://doi.org/10.1088/1361-665X/ABAA95.

[8] Ma X, Li H, Zhou S, Yang Z, Litak G. Characterizing nonlinear characteristics of asymmetric tristable energy harvesters. Mech Syst Signal Process 2022;168:108612. https://doi.org/10.1016/J.YMSSP.2021.108612.

[9] Wang W, Cao J, Zhang N, Lin J, Liao WH. Magnetic-spring based energy harvesting from human motions: Design, modeling and experiments. Energy Convers Manag 2017;132:189–97. https://doi.org/10.1016/J.ENCONMAN.2016.11.026.

[10] Margielewicz J, Gąska D, Litak G, Wolszczak P, Trigona C. Nonlinear Dynamics of a

Star-Shaped Structure and Variable Configuration of Elastic Elements for Energy Harvesting Applications. Sensors 2022, Vol 22, Page 2518 2022;22:2518. https://doi.org/10.3390/S22072518.
[11] Yang T, Cao Q. Dynamics and performance evaluation of a novel tristable hybrid energy harvester for ultra-low level vibration resources. Int J Mech Sci 2019;156:123–36. https://doi.org/10.1016/J.IJMECSCI.2019.03.034.
[12] Caetano VJ, Savi MA. Star-shaped piezoelectric mechanical energy harvesters for multidirectional sources. Int J Mech Sci 2022;215:106962. https://doi.org/10.1016/J.IJMECSCI.2021.106962.
[13] Lallart M, Zhou S, Yang Z, Yan L, Li K, Chen Y. Coupling mechanical and electrical nonlinearities: The effect of synchronized discharging on tristable energy harvesters. Appl Energy 2020;266:114516. https://doi.org/10.1016/j.apenergy.2020.114516.
[14] Liang H, Hao G, Olszewski OZ. A review on vibration-based piezoelectric energy harvesting from the aspect of compliant mechanisms. Sensors Actuators A Phys 2021;331:112743. https://doi.org/10.1016/J.SNA.2021.112743.
[15] Zhou J, Sun W, Tao Q. Gearbox low-noise design method based on panel acoustic contribution. Math Probl Eng 2014;2014. https://doi.org/10.1155/2014/850549.
[16] Zhang L, Zhang F, Qin Z, Han Q, Wang T, Chu F. Piezoelectric energy harvester for rolling bearings with capability of self-powered condition monitoring. Energy 2022;238:121770. https://doi.org/10.1016/J.ENERGY.2021.121770.
[17] Giri AM, Ali SF, Arockiarajan A. Dynamics of symmetric and asymmetric potential well-based piezoelectric harvesters: A comprehensive review. J Intell Mater Syst Struct 2020:1045389X2097829. https://doi.org/10.1177/1045389X20978292.
[18] Fu H, Mei X, Yurchenko D, Zhou S, Theodossiades S, Nakano K, et al. Rotational energy harvesting for self-powered sensing. Joule 2021;5:1074–118. https://doi.org/10.1016/J.JOULE.2021.03.006.
[19] Syta A, Litak G, Friswell MI, Adhikari S. Multiple solutions and corresponding power output of a nonlinear bistable piezoelectric energy harvester. Eur Phys J B 2016 894 2016;89:1–7. https://doi.org/10.1140/EPJB/E2016-60699-0.
[20] Zhou S, Lallart M, Erturk A. Multistable vibration energy harvesters: Principle, progress, and perspectives. J Sound Vib 2022:116886. https://doi.org/10.1016/J.JSV.2022.116886.
[21] Kumar A, Ali SF, Arockiarajan A. Enhanced Energy Harvesting from Nonlinear Oscillators via Chaos Control. IFAC-PapersOnLine 2016;49:35–40. https://doi.org/10.1016/J.IFACOL.2016.03.025.
[22] Huang Y, Zhao Z, Liu W. Systematic adjustment strategy of a nonlinear beam generator for high-energy orbit. Mech Syst Signal Process 2022;166:108444. https://doi.org/10.1016/J.YMSSP.2021.108444.
[23] Huguet T, Lallart M, Badel A. Orbit jump in bistable energy harvesters through buckling level modification. Mech Syst Signal Process 2019;128:202–15. https://doi.org/10.1016/J.YMSSP.2019.03.051.
[24] Margielewicz J, Gąska D, Litak G, Wolszczak P, Yurchenko D. Nonlinear dynamics of a new energy harvesting system with quasi-zero stiffness. Appl Energy 2022;307:118159. https://doi.org/10.1016/J.APENERGY.2021.118159.
[25] Saint-Martin C, Morel A, Charleux L, Roux E, Benhemou A, Badel A. Power expectation as a unified metric for the evaluation of vibration energy harvesters. Mech Syst Signal Process 2022;181:109482. https://doi.org/10.1016/J.YMSSP.2022.109482.

[26] Yan L, Lallart M, Karami A. Low-cost orbit jump in nonlinear energy harvesters through energy-efficient stiffness modulation. Sensors Actuators A Phys 2019;285:676–84. https://doi.org/10.1016/J.SNA.2018.12.009.
[27] Sebald G, Kuwano H, Guyomar D, Ducharne B. Experimental Duffing oscillator for broadband piezoelectric energy harvesting. Smart Mater Struct 2011;20:102001. https://doi.org/10.1088/0964-1726/20/10/102001.
[28] Wang J, Liao WH. Attaining the high-energy orbit of nonlinear energy harvesters by load perturbation. Energy Convers Manag 2019;192:30–6. https://doi.org/10.1016/J.ENCONMAN.2019.03.075.
[29] Lan C, Tang L, Qin W. Obtaining high-energy responses of nonlinear piezoelectric energy harvester by voltage impulse perturbations. Eur Phys J Appl Phys 2017;79:20902. https://doi.org/10.1051/EPJAP/2017170051.
[30] Wang J, Liao W-H, Cao J. Power enhancement of a monostable energy harvester by orbit jumps: J Intell Mater Syst Struct 2021;32:2601–14. https://doi.org/10.1177/1045389X211006912.
[31] Zhou S, Cao J, Inman DJ, Liu S, Wang W, Lin J. Impact-induced high-energy orbits of nonlinear energy harvesters. Appl Phys Lett 2015;106:093901. https://doi.org/10.1063/1.4913606.
[32] Huang Y, Liu W, Yuan Y, Zhang Z. High-energy orbit attainment of a nonlinear beam generator by adjusting the buckling level. Sensors Actuators A Phys 2020;312:112164. https://doi.org/10.1016/J.SNA.2020.112164.
[33] Margielewicz J, Gąska D, Litak G, Wolszczak P. Identification of chaotic motion zones in the QZEH system. Int. Conf. Adv. Energy Harvest. Technol. ICAEHT-2021, 2021.